ESAIM: PROCEEDINGS AND SURVEYS, October 2024, Vol. 77, p. 229-248
Emmanuel Franck, Hélène Hivert, Guillaume Latu, Hélène Leman, Bertrand Maury, Michel Mehrenberger, Laurent Navoret

HIGH ORDER NUMERICAL METHODS FOR VLASOV-POISSON MODELS OF PLASMA SHEATHS

Valentin Ayot[1], Mehdi Badsi[2], Yann Barsamian[3], Anaïs Crestetto[4], Nicolas Crouseilles[5], Michel Mehrenberger[6], Averil Prost[7] and Christian Tayou-Fotso[8]

Abstract. This article is a report of the CEMRACS 2022 project, called HIVLASHEA, standing for "**Hi**gh order methods for **Vla**sov-Poisson models for **shea**ths". A two-species Vlasov-Poisson model is described together with some numerical simulations, permitting to exhibit the formation of a plasma sheath. The numerical simulations are performed with two different methods: a first order classical finite difference (FD) scheme and a high order semi-Lagrangian (SL) scheme with Strang splitting; for the latter one, the implementation of (non-periodic) boundary conditions is discussed and different solvers for the electric field are compared. The codes are first evaluated on a one-species case, where an analytical solution is known. For the two-species case, cross-comparisons are performed and the numerical convergence of the SL method is investigated. The use of high order method is emphasized in this context. The (parallel) SL code turns out to be a robust tool to provide reliable numerical approximations of sheath stationary solution with realistic physical parameters.

Résumé. Cet article est un rapport du projet CEMRACS 2022, appelé HIVLASHEA, pour "Méthodes d'ordre élevé pour les modèles Vlasov-Poisson de gaines". Un modèle Vlasov-Poisson à deux espèces est décrit accompagné de quelques simulations numériques, permettant de mettre en évidence la formation d'un plasma gaine. Les simulations numériques sont réalisées avec deux méthodes différentes : une méthode classique du premier ordre, un schéma aux différences finies (FD) et un schéma semi-lagrangien (SL) d'ordre élevé avec splitting de Strang ; pour ce dernier cas, la mise en œuvre de conditions aux limites (non périodiques) est discutée et différents solveurs pour le domaine électrique sont comparés. Les codes sont d'abord évalués sur un cas mono-espèce, où une solution analytique est connue. Pour le cas de deux espèces, des comparaisons croisées sont effectuées et la convergence numérique de la méthode SL est étudiée. L'utilisation d'une méthode d'ordre élevé est soulignée dans ce contexte. Le code SL (parallèle) s'avère être un outil robuste pour fournir des données numériques fiables d'approximations de solution stationnaire de gaine avec des paramètres physiques réalistes.

Centre de Calcul Intensif d'Aix-Marseille is acknowledged for granting access to its high performance computing resources. This project has been supported by the French Federation for Magnetic Fusion Studies (FR-FCM)

[1] Institut de Mathématiques, CNRS, UMR 5251, Université de Bordeaux, France
[2] Nantes Université, CNRS, Laboratoire de Mathématiques Jean Leray, LMJL, UMR 6629, F-44000 Nantes, France.
[3] École européenne de Bruxelles 1, Belgique
[4] Nantes Université, CNRS, Laboratoire de Mathématiques Jean Leray, LMJL, UMR 6629, F-44000 Nantes, France.
[5] Inria (Mingus team), IRMAR UMR 6625 and ENS Rennes, Univ Rennes, France.
[6] I2M, CMI, UMR 7373, Aix-Marseille Université, France.
[7] LMI (EA 3226 - FR CNRS 3335), INSA de Rouen, France.
[8] Labo. J. A. Dieudonné, UMR 6621, Université Nice-Sophia Antipolis, France.

Article published online by EDP Sciences and available at https://www.esaim-proc.org or https://doi.org/10.1051/proc/202477229

and by the French ANR project MUFFIN ANR-19-CE46-0004. This work has been carried out within the framework of the EUROfusion Consortium, funded by the European Union via the Euratom Research and Training Programme (Grant Agreement No 101052200 EUROfusion). Views and opinions expressed are however those of the author(s) only and do not necessarily reflect those of the European Union or the European Commission. Neither the European Union nor the European Commission can be held responsible for them.
Finally, authors would like to thanks the CEMRACS organizers, Pierre Navaro for the computational support and the CIRM board.

Introduction

Plasmas have a natural tendency to remain electrically neutral. However, near a boundary, a charge imbalance may be observed in a thin layer called *sheath*. This phenomenon stems from the interaction of ions and electrons with the boundary media (a cold metallic wall, for instance). Both species will be absorbed by the wall, but with a rate proportional to their speed. Since the electrons are moving faster than the ions, a positively charged layer (the *Debye sheath*) forms near the boundary.
Plasma sheaths are particularly challenging to simulate for several reasons. In this region, the plasma parameters (temperature or density) develop steep gradients. Due to their different mass, electrons and ions have a very different behaviour close to the boundary, and a two-species model is required to dynamically describe the formation of the sheath. Moreover, kinetic models are necessary to capture the velocity effect of the particles (see [8,13,14]), and we have to deal with different scales to account for each species. Hence, we are considering in this work a two-species Vlasov model to run time dependent simulations of the plasma sheath.
Recent works are dedicated to the non homogeneous equilibrium sheath, both on the mathematical side and on the numerical side [2–4]. Regarding the dynamical approaches, one refers to [6,9] or [5] for which this study is a follow-up. In the latter work, the behaviour of the numerical solution of the Vlasov equation is studied, initialized with a sheath homogeneous equilibrium. In this work, our purpose is to investigate numerically the formation of a sheath, when we include a kinetic ionization term in the model, inspired by the recent work [1] where a fluid model is proposed. Indeed, in [1], ionization reactions are taken into account through a source term and the corresponding kinetic interpretation is considered in our Vlasov model.
Thus, we are concerned by the numerical approximation of the two-species Vlasov model including ionization and boundary conditions. To do so, we propose a high order semi-Lagrangian method combined with a time splitting method. The presence of boundaries requires specific adaptation to define correctly the high order semi-Lagrangian method close to the boundary. We adapt the strategies developed in [7,10] to define inflow and outflow ghost points according to the order of the Lagrange interpolation used in the semi-Lagrangian method. Using this strategy, a very good stability and robustness is observed for some (non necessarily physically relevant) values of mass ratio and normalized Debye length, which enables to investigate the numerical convergence of the numerical solution using parallel simulations. Moreover, different versions of Poisson equations (including boundary conditions) are compared and discussed.
The paper is organized as follows: in Section 1, we introduce the two-species Vlasov-Poisson system with boundary, the numerical methods are described in Section 2 and Section 3 is devoted to numerical results. The different codes are available respectively on https://github.com/JuliaVlasov/DynamicElectricSheath.jl for the Finite Difference solver, and on https://github.com/averil-prost/HiVlaSheaSL for the Semi-Lagrangian solver.

1. Plasma sheaths

The model. Let $t \in \mathbb{R}^+$ denote the time variable, $x \in [-1,1]$ denote the spatial variable in a normalized one-dimensional domain, and $v \in \mathbb{R}$ denote the speed variable. Each species is described through its density in the phase space, denoted by $f_i : (t,x,v) \in \mathbb{R}^+ \times [-1,1] \times \mathbb{R} \mapsto \mathbb{R}$ for the ions, and $f_e : (t,x,v) \in \mathbb{R}^+ \times [-1,1] \times \mathbb{R} \mapsto \mathbb{R}$ for the electrons. Macroscopic quantities will be needed in the modelling, so that we consider the densities $\rho_{i,e}$

and currents $J_{i,e}$ defined by

$$\rho_{i,e}(t,x) \coloneqq \int_{v\in\mathbb{R}} f_{i,e}(t,x,v)dv, \quad \text{and} \quad J_{i,e}(t,x) \coloneqq \int_{v\in\mathbb{R}} v f_{i,e}(t,x,v)dv. \tag{1.1}$$

In the sequel, we will denote $\rho(t,x) \coloneqq \rho_i(t,x) - \rho_e(t,x)$, and $J(t,x) \coloneqq J_i(t,x) - J_e(t,x)$.
Phase space densities are assumed to obey the Vlasov equation where the force term is the self-consistent electrostatic potential φ which obeys the Poisson equation. In short, the system writes

$$\begin{cases} \partial_t f_i + v\partial_x f_i - \partial_x\varphi\,\partial_v f_i = \nu f_e, & (t,x,v)\in\mathbb{R}_*^+\times(-1,1)\times\mathbb{R}, & \text{(1.2a)}\\ \partial_t f_e + v\partial_x f_e + \dfrac{\partial_x\varphi}{\mu}\,\partial_v f_e = 0, & (t,x,v)\in\mathbb{R}_*^+\times(-1,1)\times\mathbb{R}, & \text{(1.2b)}\\ -\lambda^2\partial_{xx}^2\varphi = \rho, & (t,x)\in\mathbb{R}^+\times(-1,1). & \text{(1.2c)} \end{cases}$$

The physical parameters ν, μ and λ have the following meaning:

- $\nu \geqslant 0$ is the ionization frequency. It describes the rate of creation of ions in presence of electrons.
- $\mu \coloneqq m_e/m_i$ is the mass ratio between electrons and ions.
- $\lambda > 0$ is the Debye length.

In the sequel, we may use the electric field $E(t,x) \coloneqq -\partial_x\varphi(t,x)$ instead of the potential. Then, the Poisson equation rewrites as

$$\lambda^2\partial_x E(t,x) = \rho(t,x), \qquad (t,x)\in\mathbb{R}^+\times(-1,1). \tag{1.3}$$

Remark 1.1. *To reduce the notations, we will use f_s, $s\in\{i,e\}$ to denote either the ionic or the electronic distribution. The Vlasov equations (1.2a) and (1.2b) rewrite*

$$\partial_t f_s + v\partial_x f_s - c_s\partial_x\varphi\partial_v f_s = S_s,$$

with the coefficients c_s and source terms S_s defined as

$$c_i \coloneqq 1, \quad c_e \coloneqq -\frac{1}{\mu}, \quad S_i \coloneqq \nu f_e, \quad S_e \coloneqq 0.$$

The densities f_i and f_e are subject to initial and boundary conditions, given by

$$\begin{cases} f_s(0,x,v) \coloneqq f_s^0(x,v), & (x,v)\in(-1,1)\times\mathbb{R}, & \text{(1.4a)}\\ f_s(t,x=1,v<0) = f_s(t,x=-1,v>0) \coloneqq 0, & t\in\mathbb{R}_*^+. & \text{(1.4b)} \end{cases}$$

The homogeneous boundary condition (1.4b) stems from the non-emitting wall model: the boundary absorbs particles without any reflection. This loss of ionic particles is compensated by the ionization source term in the right hand side of (1.2a). For the electrons, it is expected that the most energetic ones are absorbed by the wall, while the others are confined in the core.
To completely describe the model, we still need to provide boundary conditions for the Poisson problem (1.2c). A first one is given by the choice of a reference potential in the plasma core (at $x = 0$)

$$\varphi(t,0) = 0, \qquad \forall t\in\mathbb{R}^+. \tag{1.5}$$

To derive a second boundary condition, we introduce a symmetry assumption.

Symmetries. We will look for a symmetric potential

$$\varphi(t,x) = \varphi(t,-x), \qquad (t,x) \in \mathbb{R}^+ \times [-1,1]. \tag{1.6}$$

By derivation with respect to $x \in (-1,1)$, we immediately obtain

$$\partial_x \varphi(t,x) = -\partial_x \varphi(t,-x), \quad \text{i.e.} \quad E(t,x) = -E(t,-x).$$

In fact, assuming (1.6), the other quantities of the system also exhibit nice symmetric properties. Let us notice that the Vlasov equations (1.2a) and (1.2b) are driven by the vector fields

$$(t,x,v) \to (1, v, E(t,x)) =: V_i(t,x,v) \quad \text{and} \quad (t,x,v) \to (1, v, -E(t,x)/\mu) =: V_e(t,x,v).$$

Both these fields satisfy the radial symmetry $V_s(t,x,v) = V_s(t,-x,-v)$. In consequence, if we assume that $f_s^0(x,v) = f_s^0(-x,-v)$, the solutions $f_s(t,x,v)$ will be radially symmetric around $(t,0,0)$, i.e.

$$f_i(t,x,v) = f_i(t,-x,-v) \quad \text{and} \quad f_e(t,x,v) = f_e(t,-x,-v), \quad \forall (t,x,v) \in \mathbb{R}^+ \times [-1,1] \times \mathbb{R}.$$

In particular, we have for the densities and currents

$$\begin{aligned}
\rho_s(t,x) &= \int_{v\in\mathbb{R}} f_s(t,x,v)dv = \int_{w\in\mathbb{R}} f_s(t,x,-w)dw = \int_{w\in\mathbb{R}} f_s(t,-x,w)dw = \rho_s(t,-x),\\
J_s(t,x) &= \int_{v\in\mathbb{R}} v f_s(t,x,v)dv = -\int_{w\in\mathbb{R}} w f_s(t,x,-w)dw = -\int_{w\in\mathbb{R}} w f_s(t,-x,w)dw = -J_s(t,-x).
\end{aligned}$$

Remark 1.2 (Additional symmetry of f_e)**.** *Notice that the function $f : (t,x,v) \mapsto f_e(t,x,v) - f_e(t,x,-v)$ satisfies the linear equation*

$$0 = \partial_t f(t,x,v) + v\partial_x f(t,x,v) - \frac{E(t,x)}{\mu}\partial_v f(t,x,v).$$

The boundary condition (1.4b) gives $f(t,\pm 1, \pm v < 0) = 0$. If, in addition, we assume that the initial condition f_e^0 satisfies $f_e^0(x,v) - f_e^0(x,-v) = 0$, then we obtain

$$f_e(t,x,v) = f_e(t,x,-v), \quad \forall (t,x,v) \in \mathbb{R}^+ \times [-1,1] \times \mathbb{R}. \tag{1.7}$$

Boundary conditions. In this section, we present the different boundary conditions used to compute the electric field E to close the Poisson equation (1.2c). The common assumption of all the boundary conditions is the symmetry of the potential φ. Under the additional assumption that φ is regular, there holds the centered Neumann boundary condition

$$\partial_x \varphi(t,0) = 0 \quad \text{or equivalently} \quad E(t,0) = 0. \tag{1.8}$$

The symmetry of the field E also naturally lead to the boundary condition

$$E(t,-1) = -E(t,1), \tag{1.9}$$

as well as the integral condition

$$\int_{x=-1}^{1} E(t,x)dx = 0. \tag{1.10}$$

(1.8) to (1.10) will be compared in the numerical section. Notice that (1.8) assumes the continuity of the electric field at 0. In [11], a more elaborate boundary condition is derived using the physics of the problem. First, we derive with respect to time the Poisson equation (1.2c)

$$-\partial_t(\lambda^2\partial_{xx}^2\varphi) = \partial_t\rho,$$

and considering the difference between the v-integration of the Vlasov equations (1.2a) and (1.2b) gives (recalling $\rho = \rho_i - \rho_e$ and $J = J_i - J_e$)

$$\partial_t\rho = \nu\rho_e - \partial_x J,$$

leads to (using $E = -\partial_x\varphi$)

$$\partial_x(\lambda^2\partial_t E + J) = \nu\rho_e, \quad \forall x \in (-1,1).$$

Integrating now over $x \in [-1,1]$ leads to

$$\lambda^2\partial_t E(t,1) + J(t,1) = \lambda^2\partial_t E(t,-1) + J(t,-1) + \nu\int_{-1}^{1}\rho_e(t,x)dx, \tag{1.11}$$

and using the symmetries $E(t,1) = -E(t,-1)$ and $J(t,1) = -J(t,-1)$, it comes

$$\lambda^2\partial_t E(t,\pm1) + J(t,\pm1) = \pm\frac{\nu}{2}\int_{-1}^{1}\rho_e(t,x)dx. \tag{1.12}$$

Time integration gives a condition of the form $E(t,\pm1) = C_\pm(t)$, where

$$E(t,\pm1) = C_\pm(t) \coloneqq E(0,\pm1) - \frac{1}{\lambda^2}\int_0^t J(s,\pm1)ds \pm \frac{\nu}{2\lambda^2}\int_0^t\int_{-1}^{1}\rho_e(s,x)dxds. \tag{1.13}$$

Notice that the values $E(t,\pm1)$ now depend on the initial value $E(0,\pm1)$, whereas the centered boundary condition (1.8) does not rely on the initial state. Condition (1.13) is compared below to the simpler conditions (1.8) and (1.10).

2. Numerical methods

In this section, the numerical methods used to approximate the system (1.2) are described. First, we focus on the Poisson equation and then, two numerical methods are presented for the Vlasov part.

2.1. Poisson equation

The Poisson problem (1.2c) is solved with integral representations of the variable E. First, we consider the centered Neumann boundary condition (1.8). Then, integrating the Poisson equation (1.3) over $[0,x]$ yields

$$E(t,x) = 0 + \frac{1}{\lambda^2}\int_0^x\rho(t,y)dy = \frac{1}{\lambda^2}\int_0^x\int_{v\in\mathbb{R}}[f_i(t,y,v) - f_e(t,y,v)]dvdy. \tag{2.1}$$

Remark 2.1. *In order to use the boundary condition (1.9) or the integral condition (1.10), we compute (2.1) with an arbitrary constant and then adjust* a posteriori *to verify the chosen constraint.*

Let us now consider the boundary condition (1.13). The spatial domain $[-1,1]$ is split into its positive and negative parts, and integrating (1.3) gives

$$E(t,x) = \begin{cases} E(t,\ \ 1) - \frac{1}{\lambda^2}\int_x^1\rho(t,y)dy = C_+(t) - \frac{1}{\lambda^2}\int_x^1\int_{v\in\mathbb{R}}[f_i(t,y,v) - f_e(t,y,v)]dvdy, & x\in[0,1], \\ E(t,-1) + \frac{1}{\lambda^2}\int_{-1}^x\rho(t,y)dy = C_-(t) + \frac{1}{\lambda^2}\int_{-1}^x\int_{v\in\mathbb{R}}[f_i(t,y,v) - f_e(t,y,v)]dvdy, & x\in[-1,0). \end{cases} \tag{2.2}$$

Moreover, $C_\pm$ is computed at the required time by integrating (1.12), between two consecutive time steps. For the integrals under consideration (in space, velocity and time), we will approximate them by the trapezoidal method.

2.2. **Finite Differences (FD)**

Define a numerical computational domain $\Omega \coloneqq [-1,1] \times [-\overline{V}, \overline{V}]$, with a large enough maximum speed $\overline{V}$. Let $(x_j, v_k)_{k\in[\![0,K]\!]}^{j\in[\![0,J]\!]}$ be a cartesian grid of Ω of step $(\Delta x, \Delta v)$. We discretize the advection equations on the subgrid $(x_j, v_k)_{k\in[\![1,K-1]\!]}^{j\in[\![1,J-1]\!]}$ by an explicit Euler scheme in time, and the upwind scheme in space:

$$\frac{f_{s,j,k}^{n+1} - f_{s,j,k}^n}{\Delta t} + D_{j,k}^- f_s^n \begin{pmatrix} v_k \\ c_s E_j^n \end{pmatrix}_+ + D_{j,k}^+ f_s^n \begin{pmatrix} v_k \\ c_s E_j^n \end{pmatrix}_- = S_{s,j,k}^n, \tag{2.3}$$

where $a_+ = \max(a,0)$ and $a_- = \min(a,0)$ are respectively the element-wise positive and negative parts, and the uncentered finite differences are defined as

$$D_{j,k}^\pm f \coloneqq \pm \left(\frac{f_{j\pm1,k} - f_{j,k}}{\Delta x}, \frac{f_{j,k\pm1} - f_{j,k}}{\Delta v} \right).$$

The term E_j^n in (2.3) is an approximation of the electric field on the grid point x_j at time t^n, computed according to Section 2.1. The different boundary conditions discussed in Section 1 lead to different solvers, that will be compared in the numerical section. The values of $f_{s,j,k}^n$ on the boundary ($j = 0, J$ and $k = 0, K$) are taken as follows:

- the boundary condition (1.4b) yields $f_{s,j,k}^n = 0$ whenever $x_j = -1, v_k > 0$ or $x_j = 1, v_k < 0$,
- it is considered that $\overline{V}$ is large enough to take the values on the speed boundary $v_k = \pm\overline{V}$ equal to 0,
- the remaining values $f_{s,j,k}^n$, $x_j = -1, -\overline{V} < v_k \leqslant 0$ or $x_j = 1, 0 \leqslant v_k < \overline{V}$ may be computed using the scheme (2.3), since the sign of the speed allows to use only inner points.

The upwind scheme is stable under the CFL condition

$$1 - \max_k |v_k| \frac{\Delta t}{\Delta x} - |c_s| \max_j |E_j^n| \frac{\Delta t}{\Delta v} \geqslant 0, \quad \forall s \in \{i, e\} \text{ and } n \in [\![1, N]\!].$$

Given Δx and Δv, we deduce a sufficiently small value of Δt with the bound

$$\Delta t \leqslant \min\left(\frac{\Delta x}{\overline{V}}, \min(1,\mu) \frac{\Delta v}{E_{\max}} \right), \quad E_{\max} > 0 \text{ postulated } \textit{a priori}. \tag{2.4}$$

2.3. **Semi-Lagrangian (SL)**

The full model (1.2) nicely lends itself to approximation by time splitting. Indeed, consider the following Strang splitting decomposition

$$
\begin{aligned}
\frac{\Delta t}{2}: &\quad \begin{cases} \partial_t f_s + v\partial_x f_s = 0 & \text{Linear advection along } x, \\ \lambda^2 \partial_x E = \rho_i - \rho_e & \text{Poisson problem,} \end{cases} \\
\frac{\Delta t}{2}: &\quad \partial_t f_i = \nu f_e \qquad\qquad \text{Ionization,} \\
\Delta t: &\quad \partial_t f_s + c_s E \partial_v f_s = 0 \quad \text{Linear advection along } v, \\
\frac{\Delta t}{2}: &\quad \partial_t f_i = \nu f_e \qquad\qquad \text{Ionization,} \\
\frac{\Delta t}{2}: &\quad \begin{cases} \lambda^2 \partial_x E = \rho_i - \rho_e & \text{Poisson problem,} \\ \partial_t f_s + v\partial_x f_s = 0 & \text{Linear advection along } x. \end{cases}
\end{aligned}
$$

Each of the splitting steps may be solved exactly in time. Indeed, the Poisson problems are solved by the integral representation (2.1). The ionization steps are pointwise ODE with time-independant source term, and are exactly solved by the explicit Euler scheme. Finally, notice that each advection is at constant speed with respect to the advection variable. This allows for the use of elementary 1D solvers.
The use of the decentered boundary condition requires a discretization of (2.2), and may penalize the time order of the splitting method. In the sequel, we will consider only the symmetric boundary condition (1.8).
Numerical treatment of the boundaries. Let us focus on the elementary advection equation with constant speed $a > 0$

$$\partial_t f(t,x) + a\partial_x f(t,x) = 0, \quad f(t,-1) = 0, \quad \forall (t,x) \in \mathbb{R}_*^+ \times (-1,1).$$

Let $(x_j)_{j\in[\![0,J]\!]}$ be a space mesh of step $\Delta x \coloneqq 2/J$, and $(t_n)_{n\in[\![0,N]\!]}$ be a time mesh of step $\Delta t \coloneqq T/N$. We follow the work of [7, 10], and consider a semi-Lagrangian scheme defined as

$$f_j^{n+1} = \text{Lagrange interpolation}\,(f^n, x_j - a\Delta t) \coloneqq \sum_{k=-d}^{d+1} f_{j_0+k}^n L_k(\alpha),$$

with $(L_k)_{k\in[\![-d,d+1]\!]}$ the Lagrange polynomials of degree $(2d+1)$ defined by $L_k(z) = \prod_{\ell=-d,\ell\neq k}^{d+1} \frac{z-k}{\ell-k}$ (which satisfy $L_k(\ell) = \delta_{k\ell}$ for $\ell \in [\![-d, d+1]\!]$), and $x_j - a\Delta t = x_{j_0} + \alpha\Delta x,\ j_0 \in \mathbb{Z}, \alpha \in [0,1[$. The boundaries are treated as follows:

- the *inflow* side, corresponding to $x = -1$, relies on the analytical solution $f(t,x) = 0\ \forall x \leqslant at$. Whenever the scheme needs a value f_j^n with $j < 0$, it may be exactly taken equal to 0.
- in the case $d > 0$, the Lagrange stencil may also need *outflow* values f_j^n with $j > J$. Such values may be determined by polynomial extrapolation. Let $k_b \in \mathbb{N}$, and let p be the unique polynomial of degree k_b interpolating (x_j, f_j^n) for $j \in [\![J-k_b, J]\!]$. The *outflow ghost points* will be defined by $f_j^n \coloneqq p(-1+j\Delta x)$, $\forall j > J$. The couple (d, k_b) characterizes the chosen scheme.

3. Numerical results

The semi-Lagrangian code is written in `C`; it uses subroutines (translated from `Fortran`) of the `selalib` library[1]. The code works in parallel using `MPI`. The finite difference scheme has been written in `Julia`.

[1] https://selalib.github.io/selalib.html

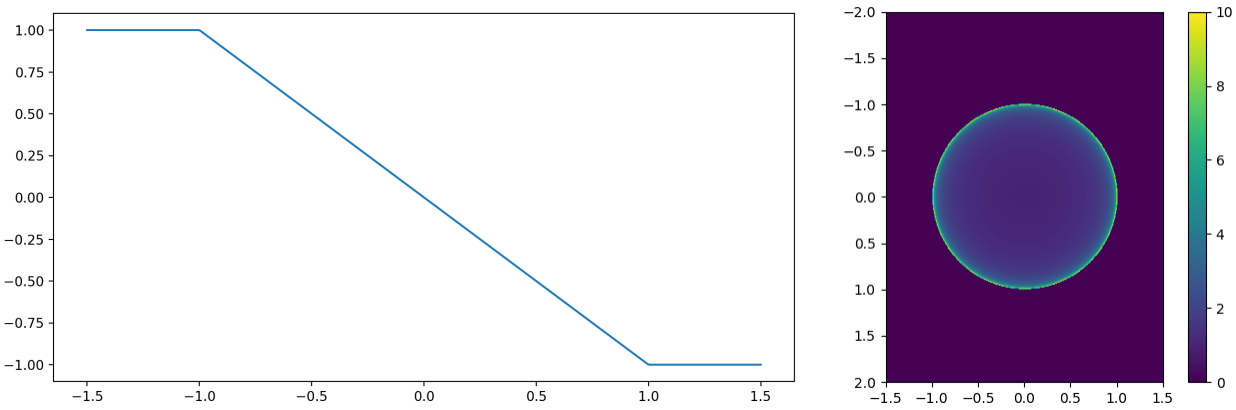

FIGURE 1. Malkov solutions (3.4) on $[-1.5, 1.5] \times [-2, 2]$. Left: electric field $E = -\partial_x \varphi$ (extended outside $[-1, 1]$ by a constant). Right: $\min(f(t = 0, x, v), 10)$ with $(x, v) \in [-1.5, 1.5] \times [-2, 2]$.

3.1. **One species validation test case**

We rely on the work of [12] to provide an analytical solution in a one-species case. Consider the simplified model describing the density of particles $f = f(t, x, v)$, and the potential $\varphi = \varphi(t, x)$:

$$\begin{cases} \partial_t f + v\partial_x f - \partial_x \varphi \partial_v f = 0, & (t, x, v) \in \mathbb{R}_*^+ \times (-1, 1) \times \mathbb{R}, \quad (3.1a) \\ \partial_{xx}^2 \varphi = \displaystyle\int_{v \in \mathbb{R}} f dv, & (t, x) \in \mathbb{R}^+ \times (-1, 1). \quad (3.1b) \end{cases}$$

The initial and boundary conditions are given by

$$\begin{cases} f(0, x, v) \coloneqq f^0(x, v), \quad f(t, x = \pm 1, \pm v < 0) = 0, & (3.2a) \\ \varphi(t, 0) = \partial_x \varphi(t, 0) = 0. & (3.2b) \end{cases}$$

This model may be seen as a particular case of the two-species Vlasov-Poisson (1.2), upon taking the following parameters:

$$f_i^0 \equiv 0, \quad \nu = 0, \quad \mu = -1, \quad \lambda = 1, \quad f_e^0 = f^0.$$

One may verify that (3.1) is solved in $\mathbb{R}^+ \times [-1, 1] \times \mathbb{R}$ by the following stationary couple:

$$f(t, x, v) \coloneqq \begin{cases} \frac{1}{\pi} \left(1 - x^2 - v^2\right)^{-1/2} & \text{if } x^2 + v^2 < 1, \\ 0 & \text{otherwise,} \end{cases} \quad \text{and} \quad \varphi(t, x) \coloneqq \frac{x^2}{2}. \quad (3.3)$$

It is numerically relevant to extend the Malkov solution (3.3) to spatial domains $x \in [-1 - \varepsilon, 1 + \varepsilon]$ by

$$f(t, x, v) \coloneqq \begin{cases} \frac{1}{\pi} \left(1 - x^2 - v^2\right)^{-1/2} & \text{if } x^2 + v^2 < 1, \\ 0 & \text{otherwise} \end{cases}, \quad \text{and} \quad \varphi(t, x) \coloneqq \begin{cases} x^2/2, & |x| < 1, \\ |x| - \frac{1}{2}, & |x| \geq 1. \end{cases} \quad (3.4)$$

Figure 1 illustrates the stationary solutions.

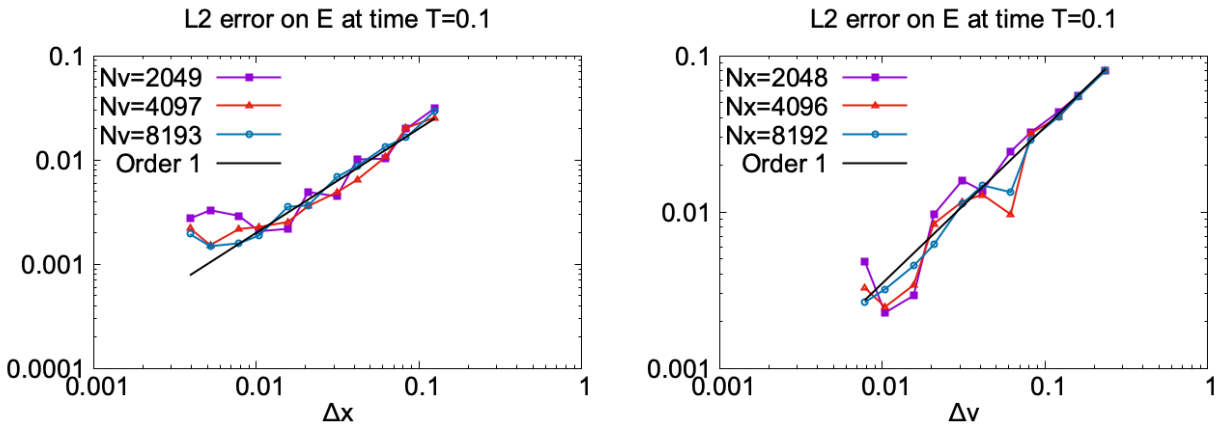

FIGURE 2. FD code for one species case. L^2-errors on electric field at time $T = 0.1$, as a function of Δx (left) or Δv (right).

Validation of the FD scheme. This stationary test first let us validate the Finite Difference scheme presented in Subsection 2.2 associated to the boundary condition (1.8) for the electric field (computed by (2.1)). Considering (x, v)-domain $[-1, 1] \times [-2, 2]$, we compute the L^2-errors on electric field at time 0.1. Figure 2 presents the error as a function of Δx for different fixed values of $N_v = K + 1$ (on the left) and as a function of Δv for different fixed values of $N_x = J + 1$ (on the right). Time step Δt is computed thanks to the CFL condition (2.4), K (resp. J) being chosen such that Δt is fixed along each curve. In both plots (presented in log-log scale), we recover convergence of rate 1, as expected, until a saturation is reached.

In Figure 3 we aim at comparing the three approaches for the computation of electric field presented in Subsection 2.1. Imposing $E(t, x = 0) = 0$ as proposed in (1.8) or $\int E(t, x)dx = 0$ as discussed in Remark 2.1 leads to two similar solutions, that are exact at $x = 0$ due to the properties of this case. Now, computing E from (1.13)-(2.2) leads to an exact solution on boundaries $x = -1$, $x = 1$ but a jump in $x = 0$. As the exact solution is continuous at $x = 0$, we consider that the solver (2.2) using the boundary condition (1.13) is unsatisfactory from a physical point of view. In the sequel, we drop this solver to focus on the simpler boundary conditions presented in Section 1.

Validation of the SL scheme. Results for the semi-Lagrangian code are given on Figure 4. Instead of evaluating the numerical solution on a point (x, v), we use a quadrature to approximate its average on the cell of size $(\Delta x, \Delta v)$ centered in (x, v). To avoid the singularity in (3.3), a finite volume interpretation of the unknown is used so that we do not have to evaluate f but instead consider its average on a cell of size $(\Delta x, \Delta v)$. We evaluate the error on the electric field for different values of $N_x = N_v = N$. We see on the left figure that the scheme converges when N increases at time $T = 0$. Then, on the right figure, we plot the error on the electric field at $T = 1$. Dividing the time step by two (resp. by four), we observe that the error is divided by around 4 (resp. 16), which illustrates the second order in time of the Strang splitting. Let us remark that the test turns out to be quite difficult, in particular since the function goes to infinity on one side and then is equal to zero on the other side, which requires large values of N to clearly see the convergence.

3.2. **Two species case**

In this part, we focus on the two-species model (1.2) and use the following physical parameters:

$$\lambda = \frac{1}{2}, \quad \mu = \frac{1}{100}, \quad \text{and} \quad \nu = 20. \tag{3.5}$$

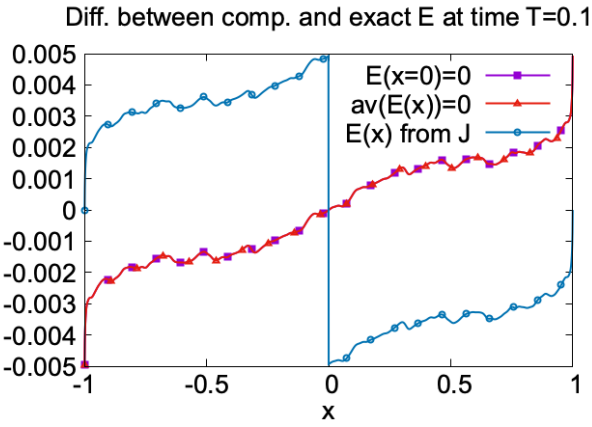

FIGURE 3. FD code for one species case. Error of the electric field as a function of $x \in [-1, 1]$ at time $T = 0.1$ using $N_x = 2048, N_v = 2049$, with three different approaches: the two approaches discussed in Remark 2.1 (imposing $E(t, x = 0) = 0$, imposing $\int_{x=-1}^{1} E(t, x)dx = 0$) and the one obtained by computing $E(t, x)$ from J with (2.2)).

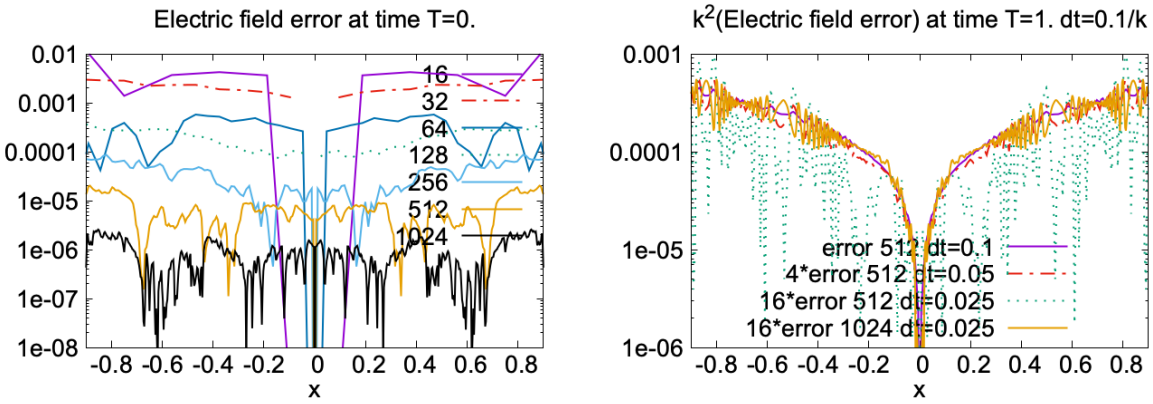

FIGURE 4. SL code for one species case. Left: error of the electric field as a function of $x \in [-1, 1]$, at time $T = 0$ using $N \in \{16, 32, 64, 128, 256, 512, 1024\}$ cells in each direction. Right: error of the electric field as a function of $x \in [-1, 1]$, at time $T = 1$, for different time steps ($\Delta t = 0.1, 0.05, 0.025$) and for different meshes ($N = 512, 1024$ cells in each direction).

The initial conditions are chosen as the thermodynamic equilibrium in an infinite spatial domain, or in a domain with periodic condition. The densities are then given by

$$f_i^0(x, v) := \frac{\exp\left(-\frac{v^2}{2}\right)}{\sqrt{2\pi}} \quad \text{and} \quad f_e^0(x, v) := \sqrt{\mu}\frac{\exp\left(-\mu\frac{v^2}{2}\right)}{\sqrt{2\pi}}. \tag{3.6}$$

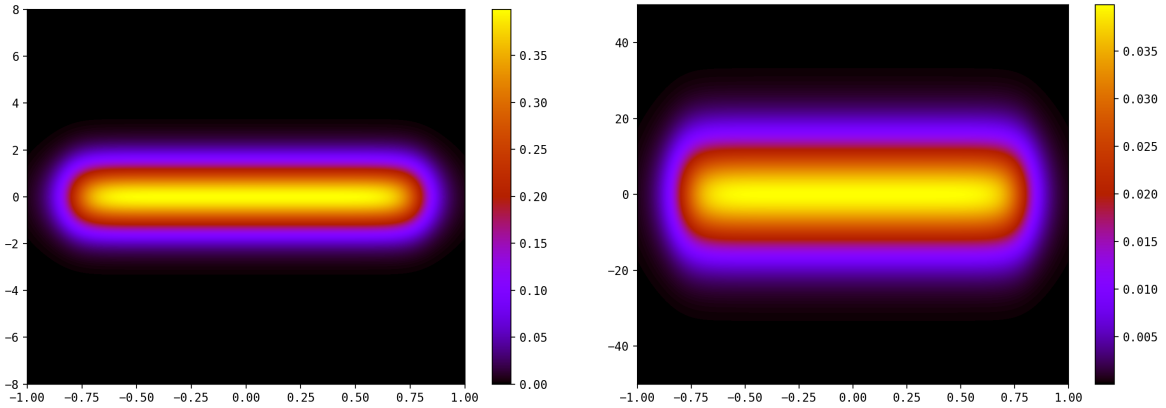

FIGURE 5. Initial conditions (3.6) f_i^0 (left) and f_e^0 (right).

In order to satisfy the boundary conditions, we multiply $f_{i,e}$ by a mask, defined as

$$\text{mask}(x, v) \coloneqq \frac{1}{2}\left(\tanh\left(\frac{x-(-0.8)}{0.1}\right) - \tanh\left(\frac{x-0.8}{0.1}\right)\right).$$

If the boundary condition is not satisfied, the sharp profile at the boundary may induce spurious oscillations in the Lagrange interpolation during the first steps of the simulation. Figure 5 illustrates the resulting initial conditions.

The simulations run over the spatial domain $x \in [-1, 1]$. The semi-Lagrangian (SL) code computes the electron velocities on $v_e \in [-60, 60]$, and ion velocities on $v_i \in [-50, 50]$. The finite differences (FD) code uses the same mesh for ions and electrons, chosen as $v \in [-60, 60]$. To simplify the comparison, visualisations of f_i are restricted to the coordinates $f_{i,j,k}$ such that $v_k \in [-5, 5]$. Note that this choice of velocity grids are required to take into account the ionization term in (1.2) which couples the ion and electron distribution functions f_i and f_e. For the finite differences code, we use $N_x = 512$, $N_{v_e} = N_{v_i} = 513$; the time step is computed in order to satisfy the CFL condition; a further time step is used for terminating to the final time T. For the semi-Lagrangian code, we will use

Run	N_x	N_{v_i}	N_{v_e}	Δt
Run0	512	513	513	0.000250
Run1	256	2049	8193	0.000250
Run2	1024	2049	8193	0.000250
Run3	1024	2049	8793	0.000025

For the SL scheme, we always use $d = 8$ with periodic boundary conditions for the interpolation in velocity, and $k_b = 1$ together with $d = 2$ for the spatial interpolation. Lagrange interpolation of degree 3 (that is, $d = 1$) is used for passing from the ion velocity mesh to the electron velocity mesh (which is needed for the ionization step).

As diagnostics, we represent the electric field E, the charge density $\rho = \rho_i - \rho_e$, the ion distribution function f_i and the electron distribution function f_e at different times $T \in \{0.1, 0.2, 1, 2, 5, 20\}$.

Comparison of boundary conditions. In Figure 6, we compare the solutions given by the semi-Lagrangian code for the different boundary conditions (1.8), (1.9) and (1.10) for the Poisson equation. Condition (1.13) is not included in the comparison, since it may produce unrealistic jumps at $x = 0$ (see the discussion of Figure 3). At the numerical level, we see that the first one $E(t, 0) = 0$ yields a loss of symmetry in the solution while the two

others preserve it. At a physical level, we observe that the electric field is monotone increasing and consequently low energetic electrons (see Figure (d)) are essentially confined while ions are prone to be accelerated and lost at the wall (see Figure (c)). In the sequel, we use the integral boundary condition (1.10).

Short time. We first look at the results for short times: $T = 0.1$ (Figure 7) and $T = 0.2$ (Figure 8). In order to compare the FD solution with a reference solution, we choose the parameters of Run2 for the SL code. Fair comparisons between FD and SL are carried for long-time simulations. We see that the results are very similar with the FD code for $T = 0.1$, which permits to validate the results by cross comparisons. For $T = 0.2$, differences begin to appear; the sharp profile of f_e is not well reproduced by the FD scheme since it is first order accurate and uses a coarser mesh whereas the high order SL enables to capture the thin structures developed by f_e. Moreover, even if the global shape of the densities ρ are similar, some differences can be observed at $x \approx \pm 0.8$.

Long time. Now, we turn to the long-term simulations, with $T = 20$, on Figure 9. Let us remark that the meshes are the same for both SL and FD (Run0). At that time $T = 20$, the finite difference code clearly suffers from numerical diffusion due its first order accuarcy: the approximations of f_i and f_e are very damped, the electric field and charge density are really different from the ones obtained by the SL scheme. Indeed, the SL scheme gives much better results (in comparison with refined runs, as we will see later), while it uses the same number of points ($N_x = N_v = 512$). Note that for the SL code, we also compare two Poisson solvers, which gives very close results. We can distinguish a little degradation of the symmetry, by looking at the charge density.

Looking for a reference solution. It is not easy to find a reference solution, as we look for long time solution, and the ionization parameter needs to be adjusted to ensure the stationarity of the solution. The space scale must be able to capture thin structures, as the Vlasov equation is prone to filamentation. We have here also the problem that electrons and ions have different time scales, which implies that short time steps have to be used in order to be able to follow the dynamics (even if we use here a semi-Lagrangian scheme, whose time step is not restricted by the strong CFL condition of the finite difference scheme).

It is interesting to notice that we can have converged solutions in space for a fixed time step, taking for example $\Delta t = 0.0025$ (or even $\Delta t = 0.025$), but the corresponding solution is then not (at all) converged in time (results are shown on Figure 10; we can remark that the results on charge density can be quite different; looking at the electron distribution function, we see some shifting of the solution, and even more changes for $\Delta t = 0.025$).

So we have diminished the time step to $\Delta t = 0.00025$, and the comparison with the same simulations with $\Delta t = 0.000025$ on Figure 11 is now much similar, which indicates that the time step is now fine enough. Note that for semi-Lagrangian schemes, taking the smallest possible time step does not necessarily lead to a better result (due to accumulation of errors, as the number of interpolations increases).

We choose to use a very fine discretization in velocity for the electrons by taking $N_{v_e} = 8193$ (some results, not shown, with $N_{v_e} = 16385$ have lead to indistinguishable results). We then vary N_x and N_{v_i}; we remark that N_x can be quite lower and N_{v_i} a little lower also, as we have similar results taking $(N_x, N_{v_i}) = (256, 2049)$ and $(N_x, N_{v_i}) = (1024, 4097)$, as we can see on Figure 12 (the first one is more diffusive which is coherent).

We observe also that the spatial interpolation does not lead to unstable results, which can occur sometimes when extrapolation is used (see [5]). To our understanding, this is due to the fact that interpolation of non-trivial functions happens only on the outflow boundary, and any oscillation is evacuated immediately without propagation in the computational domain. We have used an odd number of points in order to prevent from having 0 as a mesh point, which would lead to increase of the value at constant rate, in the ionization step.

The study of the numerical equilibrium and the study of the behaviour of the ion density around $(0, 0)$, which is quite complex at equilibrium, are not tackled here and are out of the scope of this work.

4. Conclusion

This work discussed the development of a semi-Lagrangian scheme for the numerical simulation of a two-species plasma model involving sheath. Specific treatment of the boundary conditions have been proposed. For comparison, a first order finite difference scheme has been implemented. Both schemes are first validated

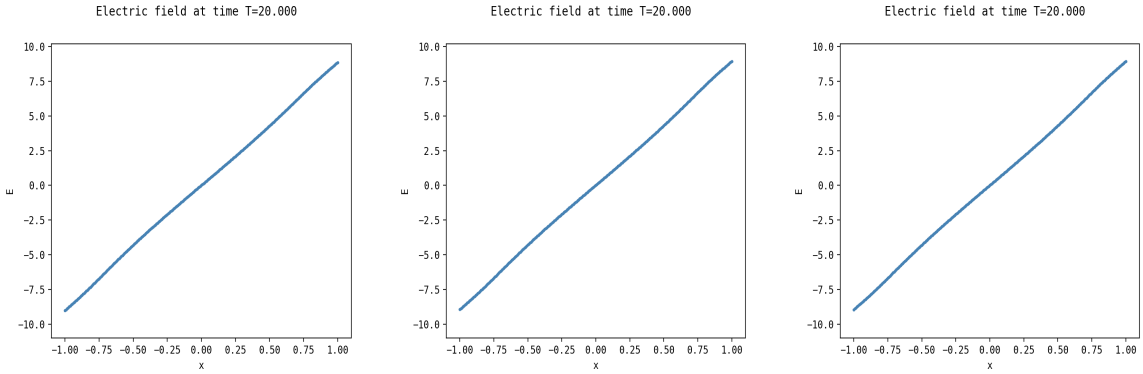

(A) Electric field

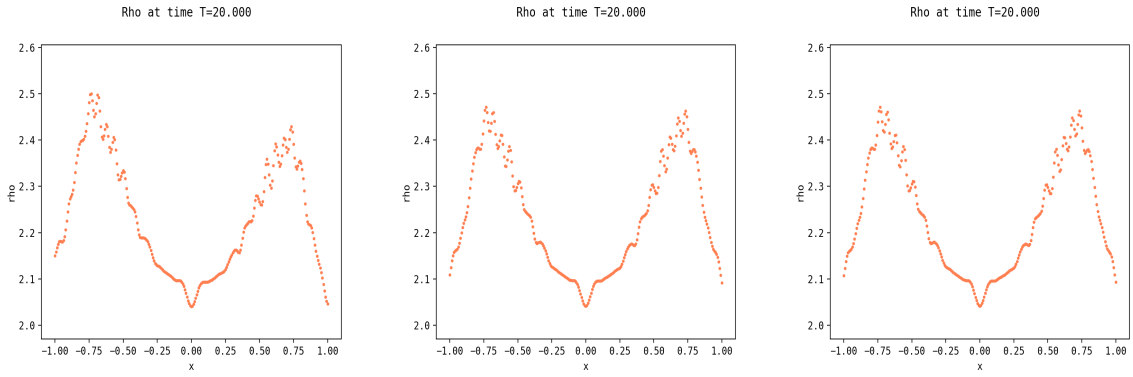

(B) Density ρ

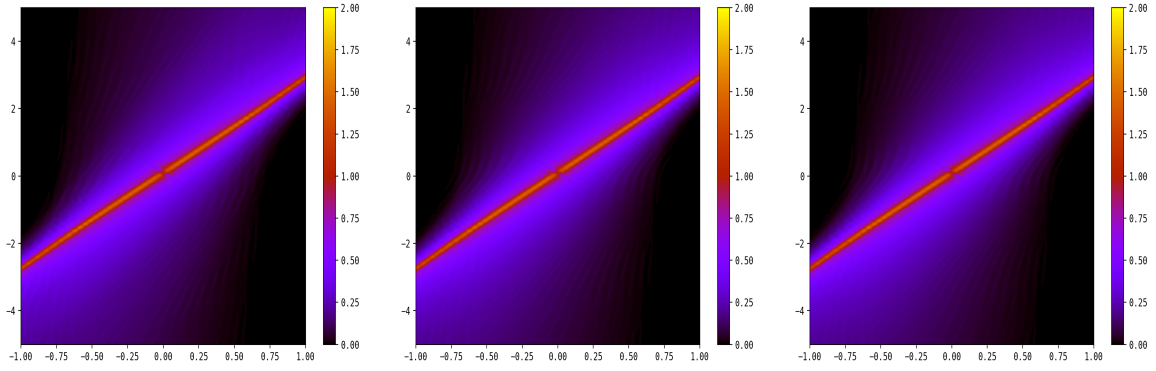

(C) Ion distribution function

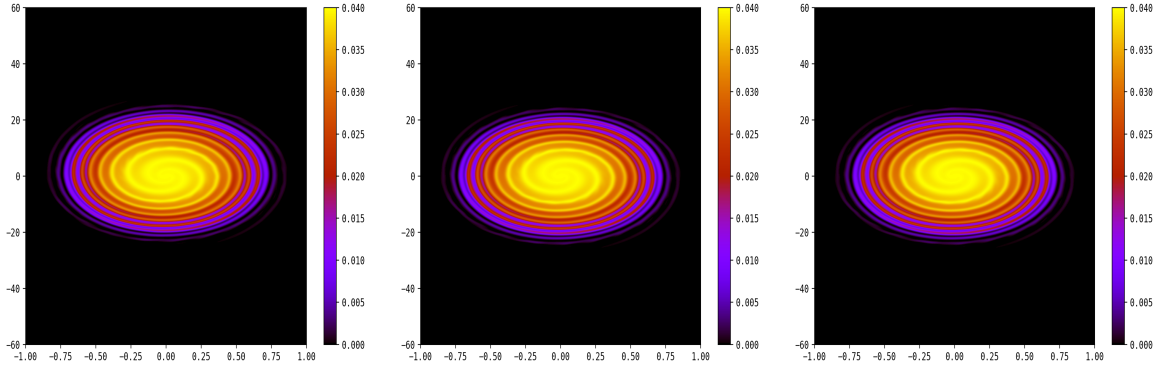

(D) Electron distribution function

FIGURE 6. Comparison of the numerical approximation of the Poisson equation in the semi-

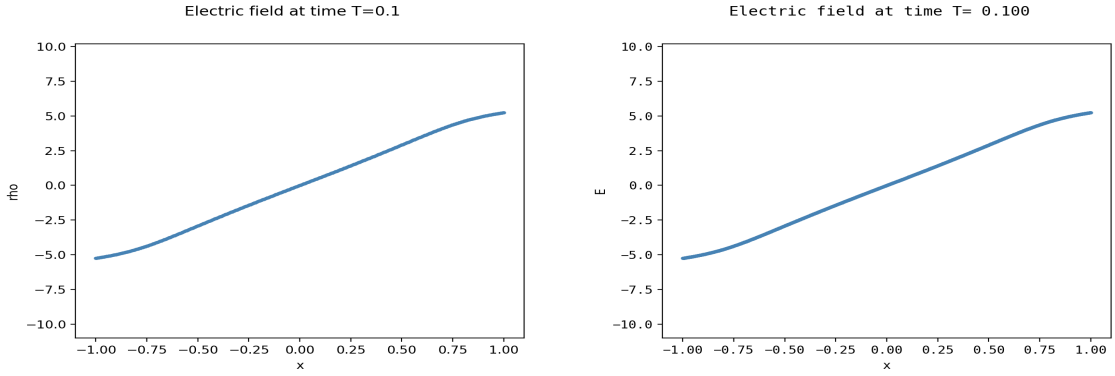

(A) Electric field

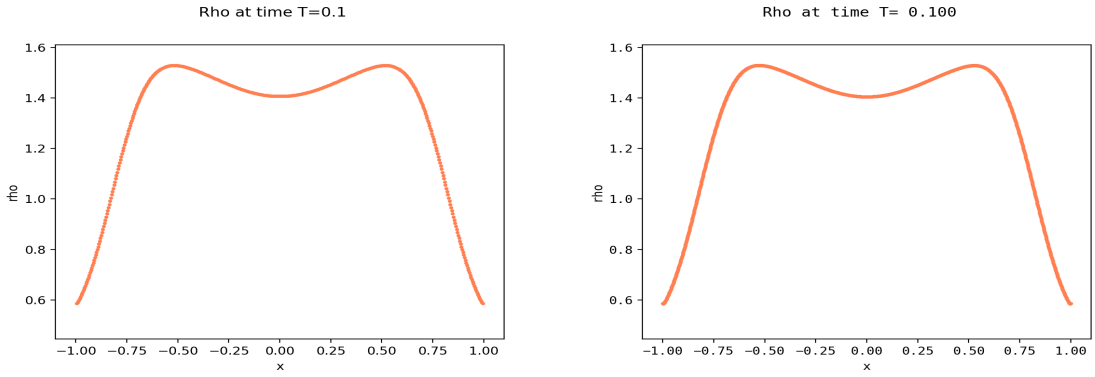

(B) Density ρ

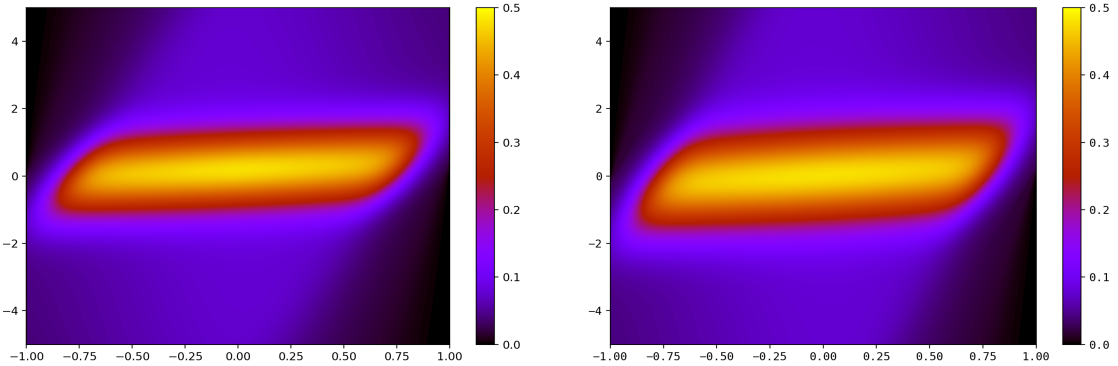

(C) Ion distribution function

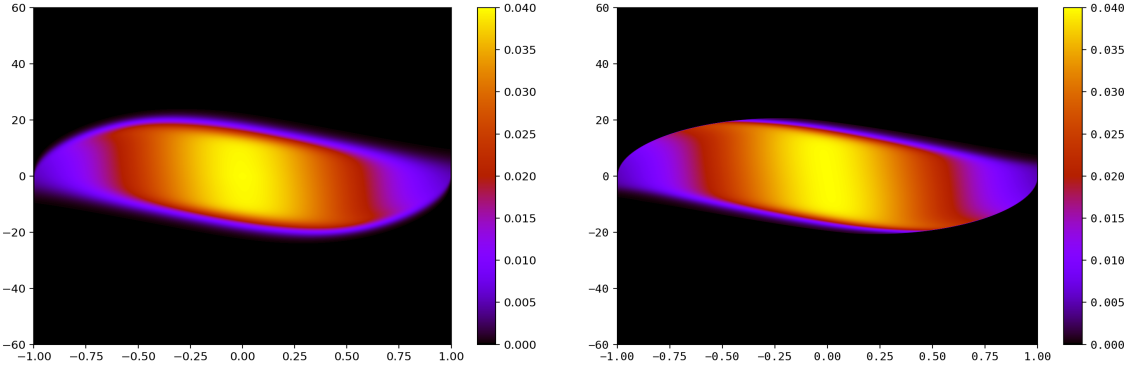

(D) Electron distribution function

FIGURE 7. Comparison between finite differences (left) and semi-Lagrangian (right) schemes at $T = 0.1$. The semi-Lagrangian code uses parameters of Run2.

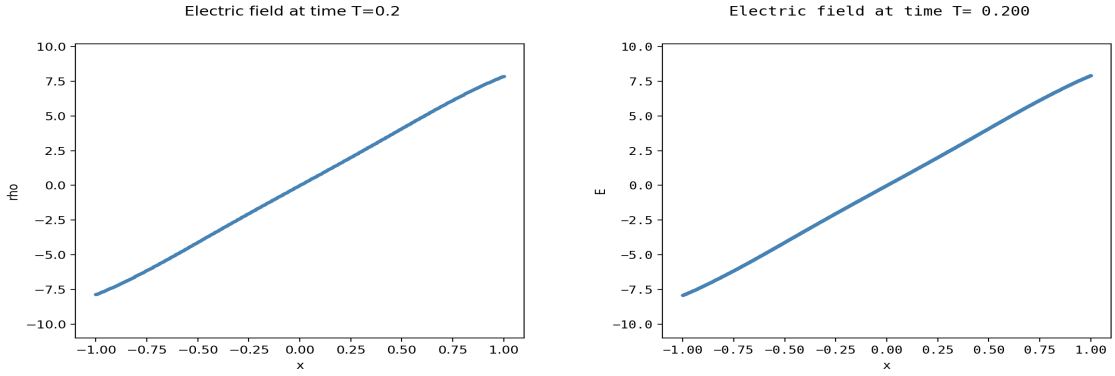

(A) Electric field

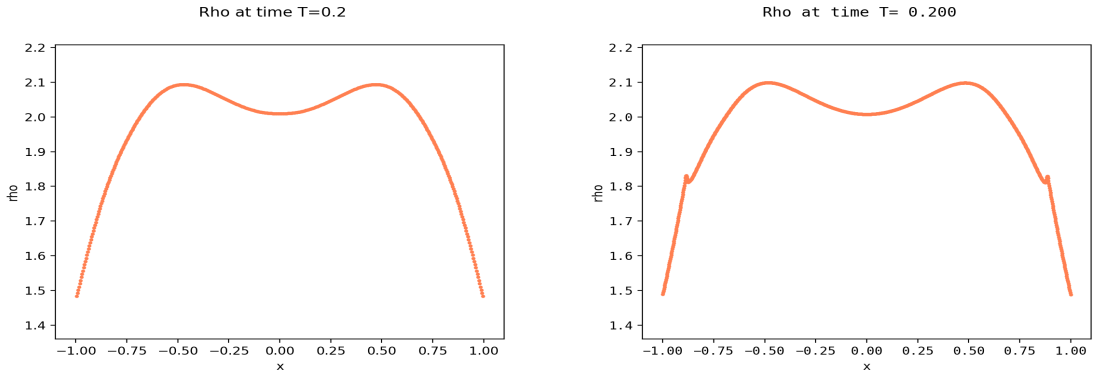

(B) Density ρ

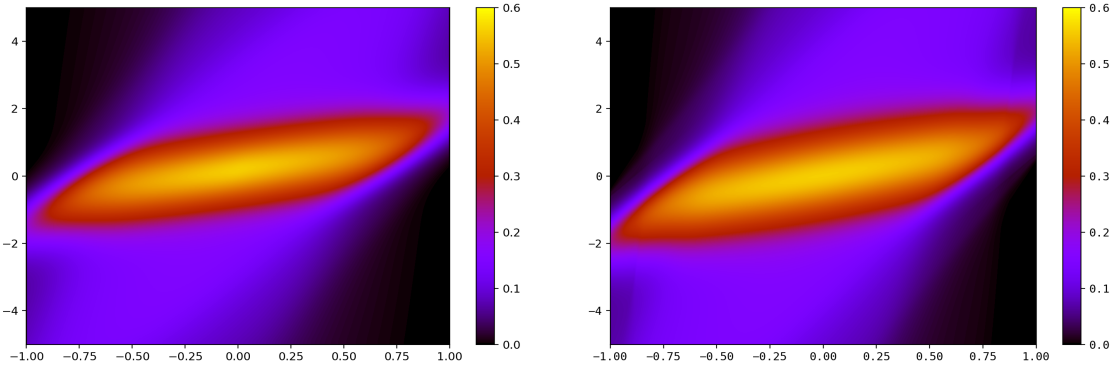

(C) Ion distribution function

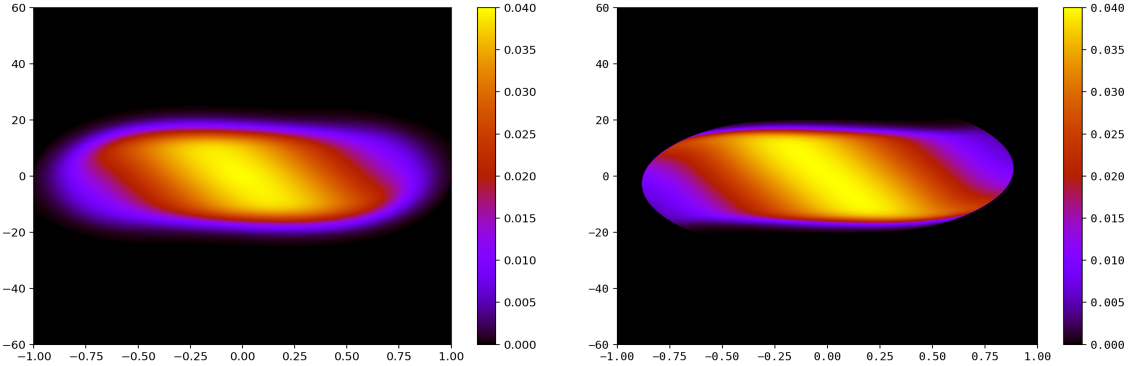

(D) Electron distribution function

FIGURE 8. Comparison between finite differences (left) and semi-Lagrangian (right) schemes at $T = 0.2$. The semi-Lagrangian code uses parameters of Run2.

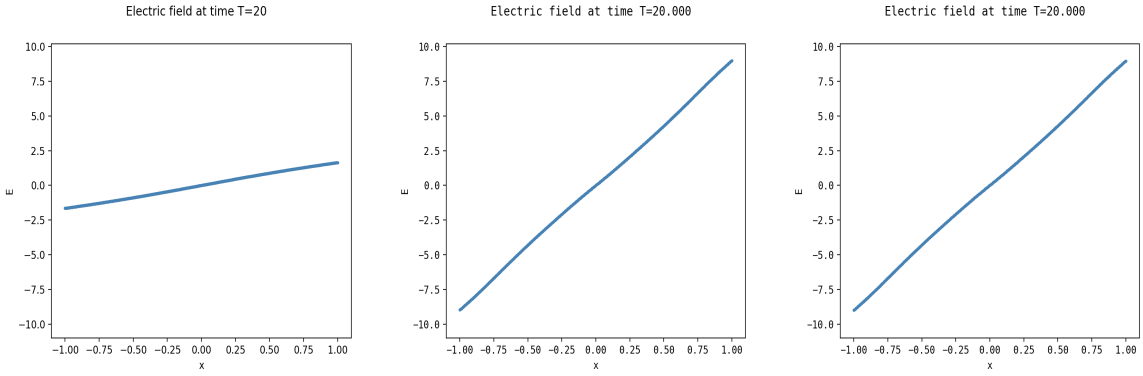

(A) Electric field

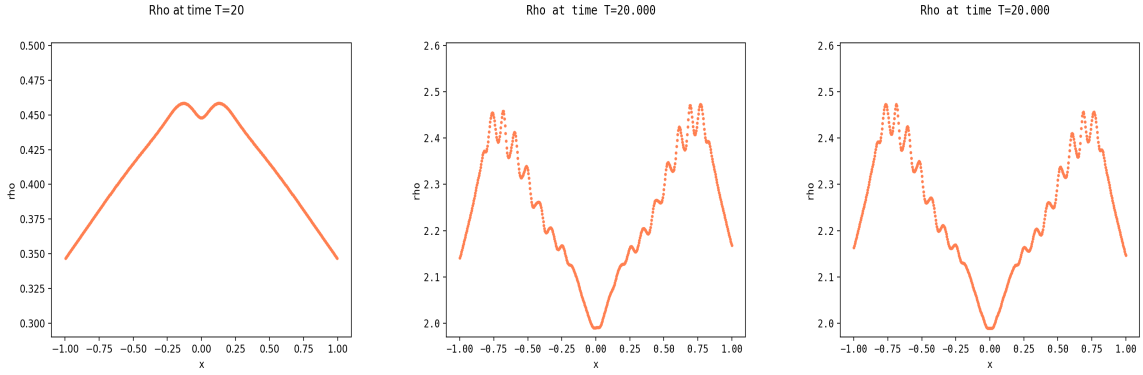

(B) Density ρ

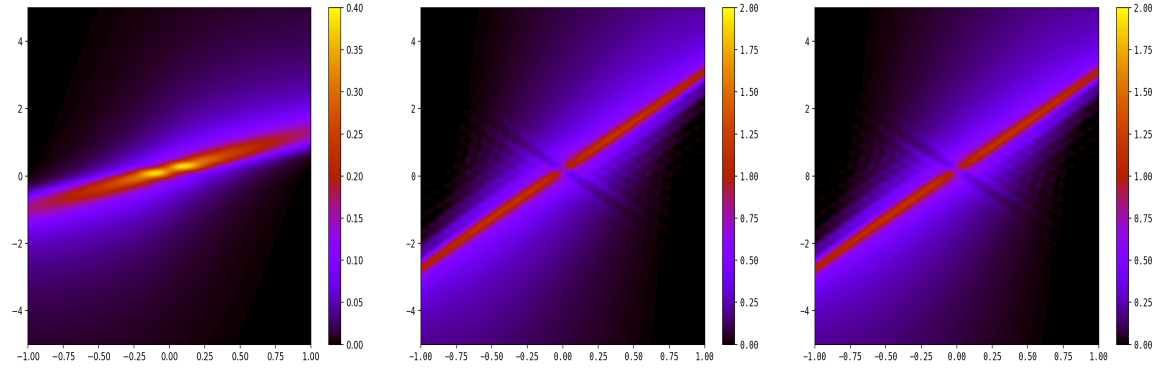

(C) Ion distribution function

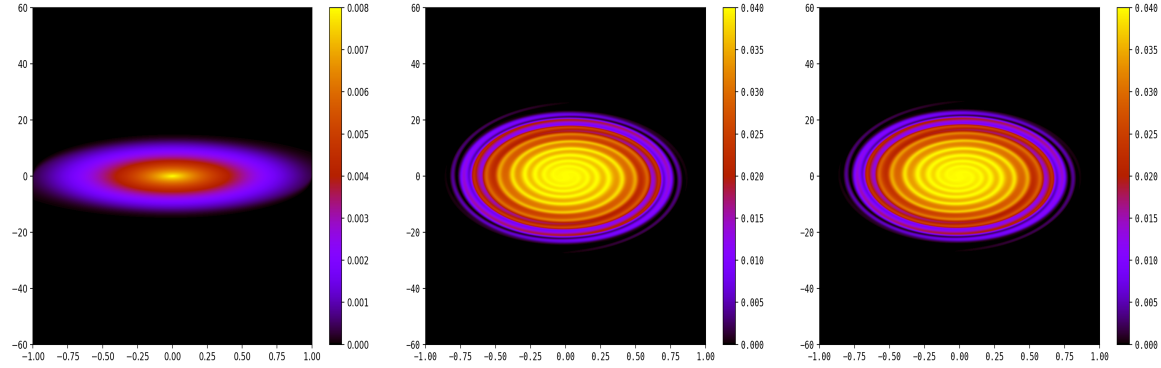

(D) Electron distribution function

FIGURE 9. Comparison between finite differences (left) and semi-Lagrangian (middle and right) schemes at $T = 20$. The semi-Lagrangian code uses parameters of Run0 (middle $E(t,0) = 0$

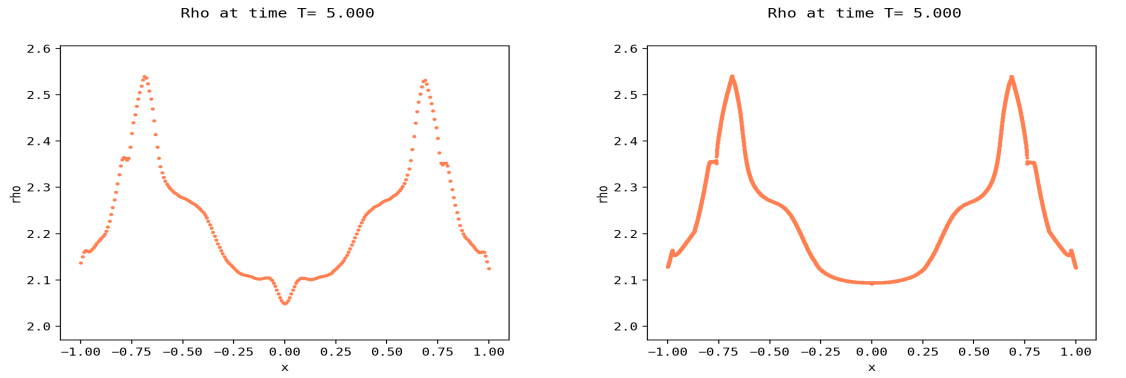

(A) ρ for $\Delta t = 0.025$. $N_x = 256, N_{v_e} = N_{v_i} = 1023$ (left): $N_x = 4096, N_{v_e} = 8193,\ N_{v_i} = 16385$ (right)

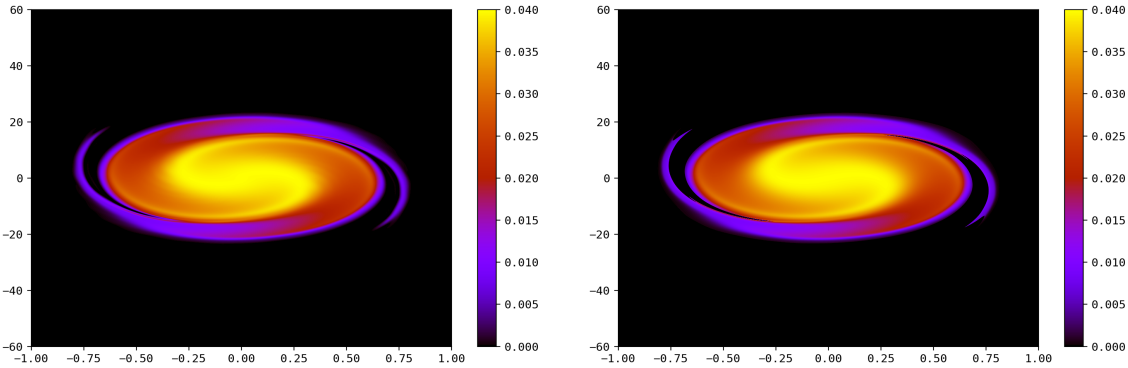

(B) f_e for $\Delta t = 0.025$. $N_x = 256, N_{v_e} = N_{v_i} = 1023$ (left): $N_x = 4096, N_{v_e} = 8193,\ N_{v_i} = 16385$ (right)

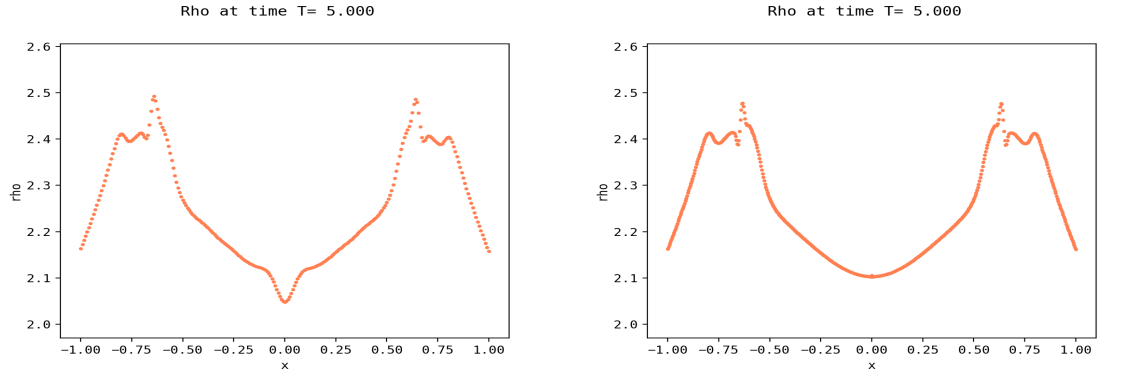

(C) ρ for $\Delta t = 0.0025$. $N_x = 256, N_{v_e} = N_{v_i} = 1023$ (left): $N_x = 512, N_{v_e} = N_{v_i} = 8193$ (right)

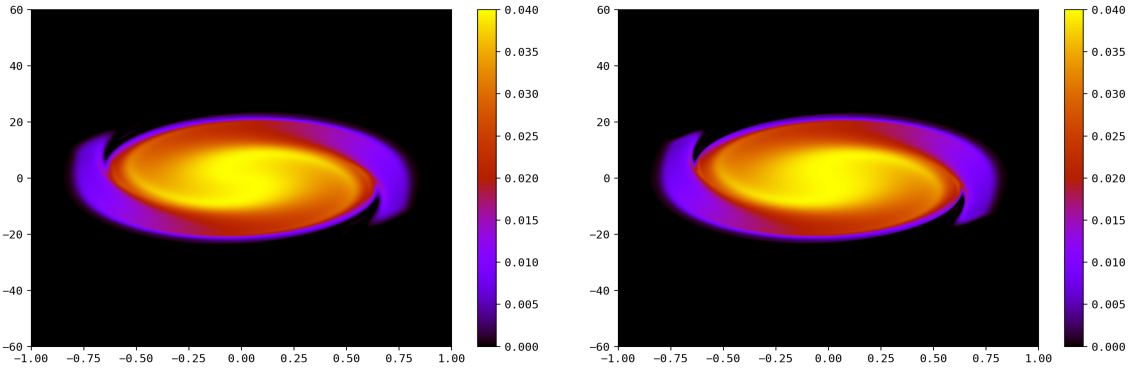

(D) ρ for $\Delta t = 0.0025$. $N_x = 256, N_{v_e} = N_{v_i} = 1023$ (left): $N_x = 512, N_{v_e} = N_{v_i} = 8193$ (right)

FIGURE 10. Density ρ and electron distribution function f_e for time $T = 5$, with $\Delta t = 0.025$ and $\Delta t = 0.0025$. The semi-Lagrangian code is used: coarse mesh on the left and fine mesh on

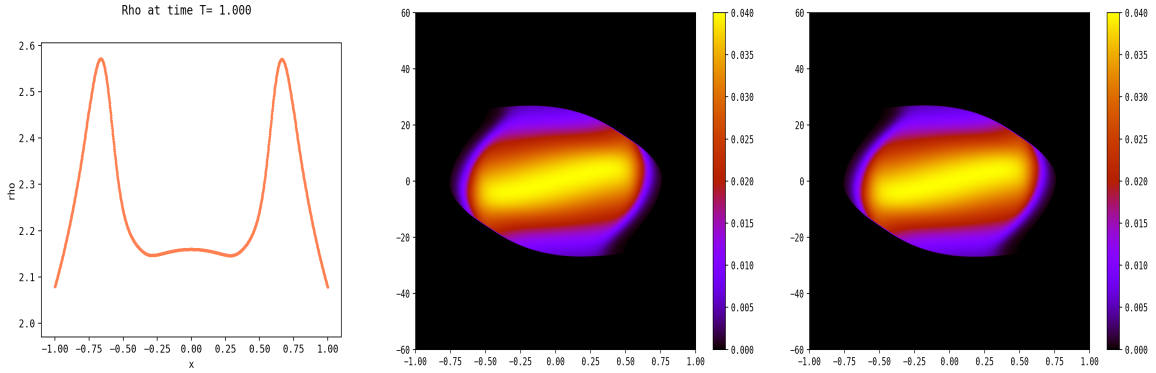

(A) $T = 1$

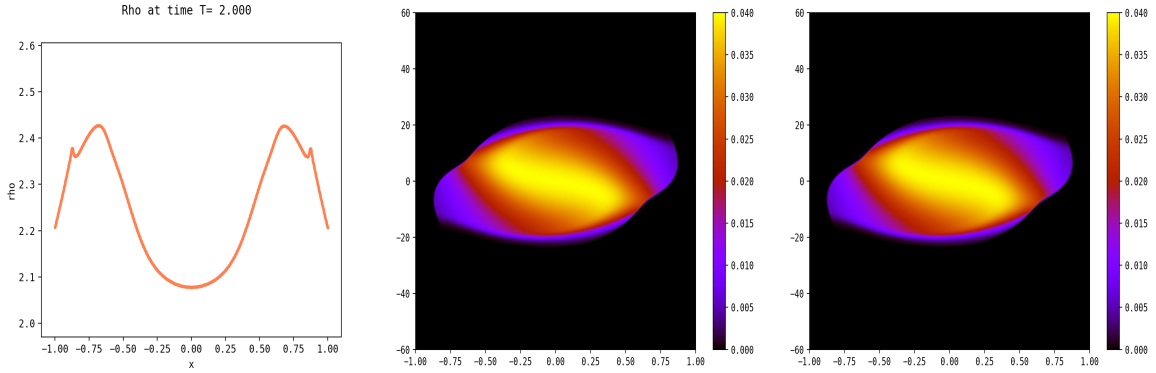

(B) $T = 2$

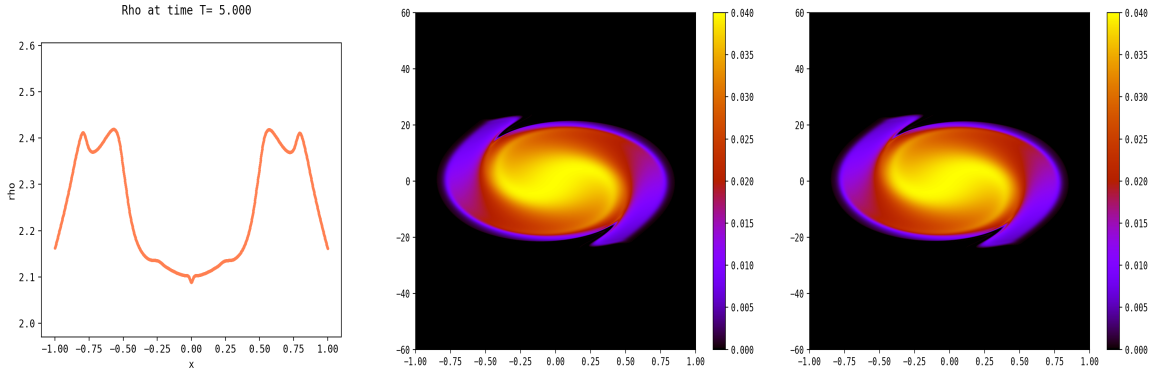

(C) $T = 5$

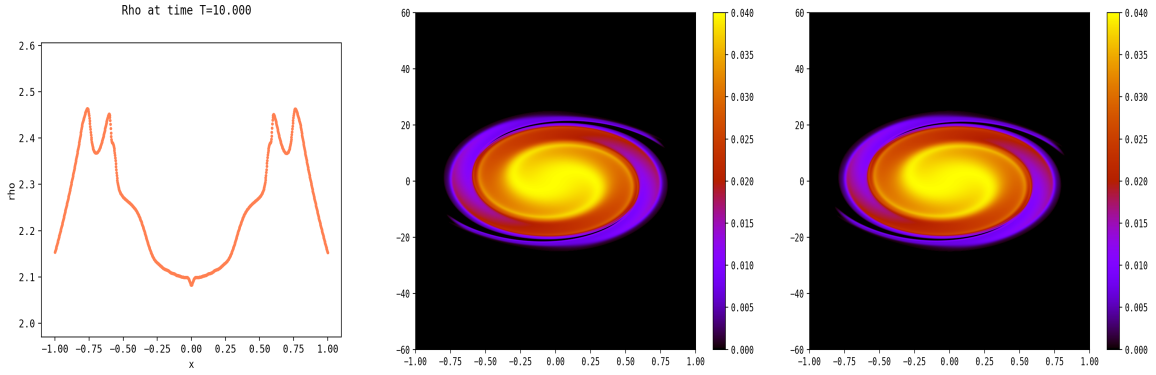

(D) $T = 10$

FIGURE 11. Density ρ (left) and electron distribution function (middle and right) for time $T \in \{1, 2, 5, 10\}$. The semi-Lagrangian code is used with parameters of Run2 (left, middle) and

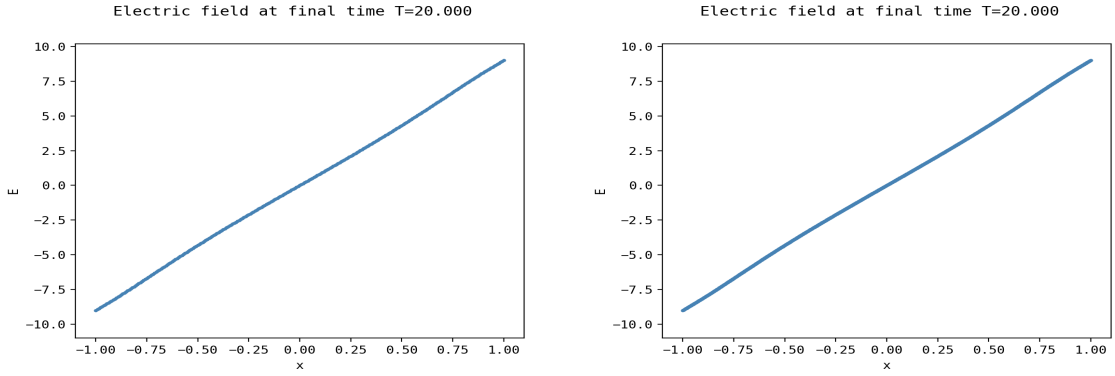

(A) Electric field

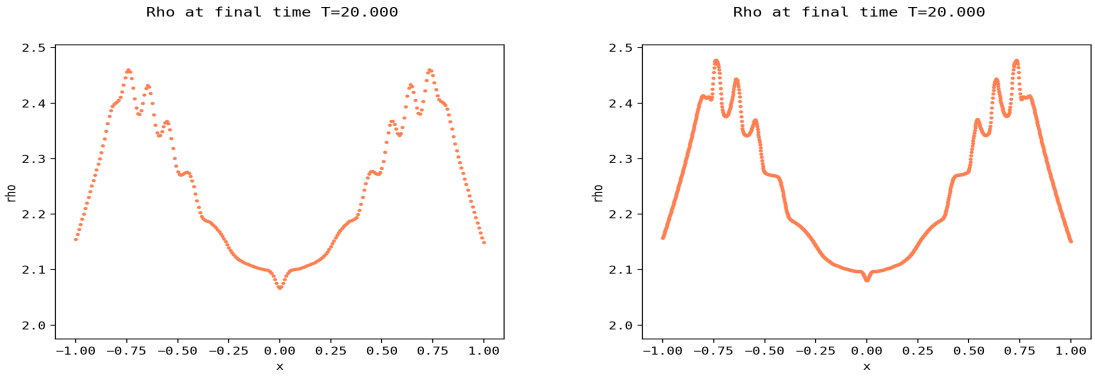

(B) Density ρ

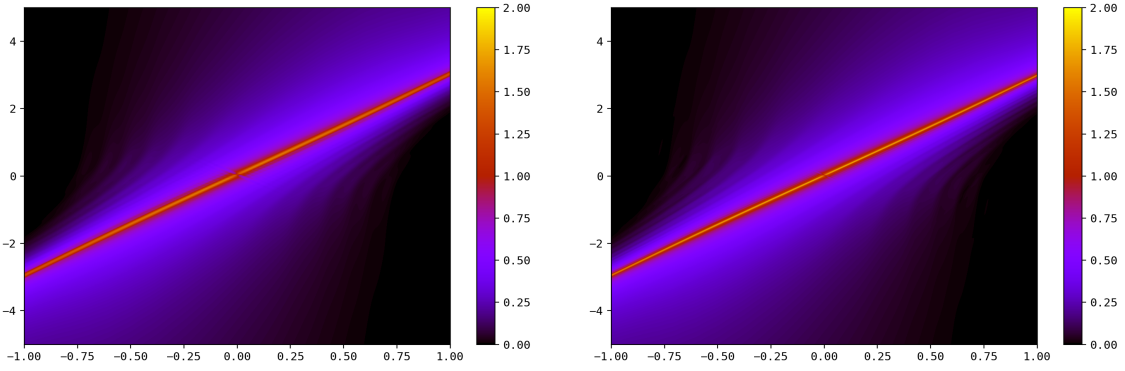

(C) Ion distribution function

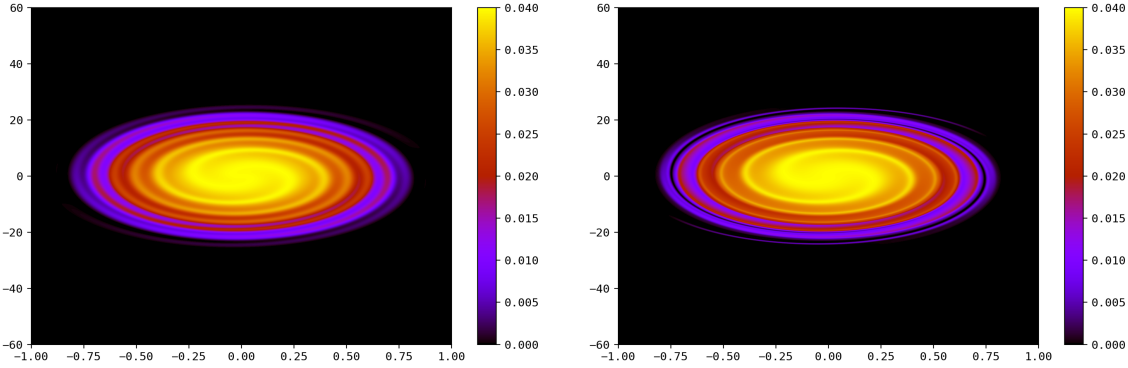

(D) Electron distribution function

FIGURE 12. Comparison of semi-Lagrangian code: parameters of Run1 (left column) and parameters of Run2 (right column).

on a one-species test case for which an analytic solution is known. Then we obtained simulations for the full two-species case.

Promising results on the formation of sheath solution are obtained, which encourages us to go further in the study of this semi-Lagrangian scheme coupled with boundary conditions. The robustness of the parallel SL code enables to investigate the numerical convergence of the sheath solution. The SL code turns out to be a good tool to study stationary sheath solutions even if the long-time behaviour of the solution to (1.2) is a difficult question for which it would be very interesting to have a reference solution, given by the stationary problem. This is however out of the scope of this work.

References

[1] A. Alvarez Laguna, T. Pichard, T. Magin, P. Chabert, A. Bourdon, and M. Massot. An asymptotic preserving well-balanced scheme for the isothermal fluid equations in low-temperature plasmas at low-pressure. *Journal of Computational Physics*, 419:109634, October 2020.

[2] Mehdi Badsi. Collisional sheath solutions of a bi-species Vlasov-Poisson-Boltzmann boundary value problem. *Kinetic & Related Models*, 14(1):149, 2021.

[3] Mehdi Badsi, Christophe Berthon, and Anaïs Crestetto. A stable fixed point method for the numerical simulation of a kinetic collisional sheath. *Journal of Computational Physics*, 429:109990, March 2021.

[4] Mehdi Badsi, Martin Campos Pinto, and Bruno Després. A minimization formulation of a bi-kinetic sheath. *Kinetic and Related Models*, 9(4):621–656, September 2016.

[5] Mehdi Badsi, Michel Mehrenberger, and Laurent Navoret. Numerical stability of plasma sheath. *ESAIM: Proceedings and Surveys, SMAI 2017*, 64:17–36, 2018.

[6] Emily Bourne, Yann Munschy, Virginie Grandgirard, Michel Mehrenberger, and Philippe Ghendrih. Non-Uniform Splines for Semi-Lagrangian Kinetic Simulations of the Plasma Sheath. *Journal of Computational Physics*, 488:112229, 2023.

[7] B. Boutin, T.H.T. Nguyen, A. Sylla, S. Tran-Tien, and J.-F. Coulombel. High order numerical schemes for transport equations on bounded domains. *ESAIM: Proceedings and Surveys*, 70:84–106, 2021.

[8] Petr Cagas. *Continuum Kinetic Simulations of Plasma Sheaths and Instabilities*. PhD thesis, Virginia Tech, 2018.

[9] David Coulette and Giovanni Manfredi. An Eulerian Vlasov code for plasma-wall interactions. *Journal of Physics: Conference Series*, 561(1), November 2014.

[10] Jean-François Coulombel and Frédéric Lagoutière. The Neumann numerical boundary condition for transport equations. *Kinetic & Related Models*, 13(1):1–32, 2020.

[11] Stephane Devaux and Giovanni Manfredi. Magnetized plasma-wall transition consequences for wall sputtering and erosion. *Plasma Physics and Controlled Fusion*, 50:025009, January 2008.

[12] Evgeny A. Malkov and Alexey N. Kudryavtsev. Non-stationary Antonov self-gravitating layer: Analytics and numerics. *Monthly Notices of the Royal Astronomical Society*, 491:3952–3966, January 2020.

[13] K.-U. Riemann. The Bohm criterion and sheath formation. *Journal of Physics D: Applied Physics*, 24(4):493, April 1991.

[14] Guang-Yu Sun, Shu Zhang, Bao-Hong Guo, An-Bang Sun, and Guan-Jun Zhang. Vlasov simulation of the emissive plasma sheath with energy-dependent secondary emission coefficient and improved modeling for dielectric charging effects. *Frontiers in Physics*, 10, 2022.